Electronic Supplementary Information

Direct observation of a ferri-to-ferromagnetic transition in a fluoride-bridged 3d-4f molecular cluster

Jan Dreiser,*[a] Kasper S. Pedersen,*[b] Cinthia Piamonteze,[a] Stefano Rusponi,[c] Zaher Salman,[d] Md. Ehesan Ali,[e] Magnus Schau-Magnussen,[b] Christian Aa. Thuesen,[b] Stergios Piligkos,[b] Høgni Weihe,[b] Hannu Mutka,[f] Oliver Waldmann,[g] Peter Oppeneer,[h] Jesper Bendix,*[b] Frithjof Nolting,[a] and Harald Brune[c]

[a] *Swiss Light Source, Paul Scherrer Institut, CH-5232 Villigen PSI, Switzerland. E-mail: jan.dreiser@psi.ch*

[b] *Department of Chemistry, University of Copenhagen, DK-2100 Copenhagen, Denmark. E-mail: ksp@kiku.dk (K.S.P.), bendix@kiku.dk (J.B.)*

[c] *Institute of Condensed Matter Physics, Ecole Polytechnique Fédérale de Lausanne, CH-1015 Lausanne, Switzerland.*

[d] *Laboratory for Muon Spin Spectroscopy, Paul Scherrer Institut, CH-5232 Villigen PSI, Switzerland.*

[e] *Center for Theoretical Chemistry, Ruhr-Universität Bochum, D-44801, Bochum, Germany.*

[f] *Institut Laue-Langevin, F-38042 Grenoble Cedex 9, France.*

[g] *Physikalisches Institut, Universität Freiburg, D-79104 Freiburg, Germany.*

[h] *Department of Physics and Astronomy, Uppsala University, Box 516, S-751 20 Uppsala, Sweden.*

.

Table of contents

Experimental Section

General Procedures and Materials

All chemicals and solvents were purchased from commercial sources and used without further purification. $[Dy(hfac)_3(H_2O)_2]$ and *trans*-$[CrF_2(py)_4]NO_3$ were prepared as described in the literature.[1]

Syntheses

Synthesis of 1: To a solution of $[Dy(hfac)_3(H_2O)_2]$ (4.0 g, 4.9 mmol) in chloroform (60 ml, LabScan; stabilized by 1% ethanol) was added a solution of *trans*-$[CrF_2(py)_4]NO_3$ (0.5 g, 1.0 mmol) in chloroform (10 ml). The resulting solution was left standing for 12 h to yield needles of $[Dy(hfac)_3(H_2O)–CrF_2(py)_4–Dy(hfac)_3(NO_3)]$ which were filtered off and washed with chloroform. Yield: 62% (based on Cr). *Anal. Calc.* (found) for $H_{28}C_{50}N_5O_{16}F_{38}CrDy_2$: C: 29.24% (29.13%), H: 1.37% (1.26%), N: 3.41% (3.33%)

Synthesis of 2: To a solution of *trans*-$[CrF_2(py)_4]NO_3$ (1.2 g, 2.6 mmol) in chloroform (25 ml) was added a solution of one equivalent $[Dy(hfac)_3(H_2O)_2]$ (2.1 g, 2.6 mmol) in chloroform (40 ml). Red-violet, block-shaped crystals of $[Dy(hfac)_4–CrF_2(py)_4]\cdot ½CHCl_3$ were filtered off after several hours and washed with successive aliquots of chloroform. The samples were stored in closed vials in a freezer to suppress solvent loss. Yield: 36% (based on Cr), *Anal. calc.* (found) for $H_{24.5}C_{40.5}N_4O_8F_{26}Cl_{1.5}CrDy$: C: 33.39% (33.02%), H: 1.70% (1.49%), N: 3.85% (3.90%).

Crystallography

Single-crystal X-ray diffraction data were acquired at 122 K on a Nonius KappaCCD area-detector diffractometer, equipped with an Oxford Cryostreams low-temperature device, using graphite-monochromated Mo Kα radiation (λ = 0.71073 Å). The structures were solved using direct methods (SHELXS97) and refined using the SHELXL97 software package.[2] All non-hydrogen atoms were refined anisotropically, whereas H-atoms were isotropic and constrained. Crystal structure and refinement data for **1** and **2** are summarised in Table S1. The structure of **2** contains a highly disordered solvent $CHCl_3$ molecule and no satisfactory model that describes this solvent could be achieved. Hence the PLATON SQUEEZE[3] procedure was used in the refinement to calculate a solvent-accessible void of 311 $Å^3$. It was confirmed that the disordered solvent is located in the void volume.

	1	**2**
Formula	$C_{50}H_{28}CrDy_2F_{38}N_5O_{16}$	$C_{40}H_{24}CrDyF_{26}N_4O_8$
M_r	2053.77	1397.13
Color, shape	Pink, prism	Pink, prism
crystal size/mm	0.45 × 0.10 × 0.09	0.36 × 0.18 × 0.09
Crystal system	Monoclinic	triclinic
Space group	*C*2/*c*	P-1
T/K	122	122
a/Å	26.3208 (13)	12.515 (5)
b/Å	15.7874 (15)	19.836 (7)
c/Å	18.718 (3)	21.392 (6)
α/°	90	85.52 (3)
β/°	115.474 (9)	81.35 (4)
γ/°	90	86.229 (19)
V/Å^3	7021.9 (13)	5226 (3)
Z	4	4
ρ_{calc}/g cm^{-3}	1.943	1.776
F_{000}	3956	2720
μ(Mo *K*α)/mm^{-1}	2.42	1.77
θ range/°	1.6–27.5	1.0–35.0
collected reflns	73764	299677
unique reflns	8074	45853
params/restraints	534/3	1441/0
reflns ($I > 2\sigma(I)$)	6301	33140
GoF	1.07	1.04
$R1^a$($I > 2.00\sigma(I)$)	0.041	0.043
$R1^a$(all data)	0.062	0.073
$wR2^b$(all data)	0.107	0.095
max/min $\Delta\rho$/e Å^{-3}	1.56/−0.84	1.69/−1.27

[a] $R1 = \Sigma||F_o| - |F_c||/\Sigma|F_o|$. [b] $wR2 = [\Sigma w(F_o^2 - F_c^2)^2/\Sigma w(F_o^2)^2]^{1/2}$

Table S1: Crystallographic data of **1** and **2**.

SQUID magnetometer measurements

The magnetic characterisation was performed on a Quantum-Design MPMS-XL SQUID magnetometer equipped with a 5 T dc magnet. The polycrystalline samples were enclosed in frozen *n*-eicosane in polycarbonate capsules. The temperature dependence of the dc magnetic susceptibility was determined from magnetisation measurements from 1.8 K to 300 K in a dc field of 100 mT. Magnetisation data were acquired at fields up to 5 T and at different temperatures. Data were

corrected for diamagnetic contributions from the sample, *n*-eicosane and the sample holder by means of Pascal´s constants. Ac susceptibility measurements were carried out using an oscillating field of 0.3 mT and static dc fields of up to 1 T.

X-ray magnetic circular dichroism

X-ray magnetic circular dichroism (XMCD) measurements were performed at the X-Treme beamline at the Swiss Light Source, Paul Scherrer Institut, Switzerland. To prepare the sample, polycrystalline powder of **1** was pressed into a piece of Indium mounted on a sample holder. X-ray absorption spectra were recorded at a temperature of 2 K in total electron yield mode at the Dy $M_{4,5}$ and Cr $L_{2,3}$ edges. Magnetic fields of up to $B = \pm 6$ T along the beam propagation direction were applied. The beam was defocused (spot size $\sim 1 \times 1$ mm^2) and kept at very low intensity to avoid radiation damage. Scans were taken "on-the-fly", i.e. the monochromator and insertion device were moving continuously while the data were acquired.[4] To obtain magnetisation curves, a full magnetic-field loop was performed at one polarisation while measuring X-ray absorption at the energy of maximum dichroism and at the baseline. Hereafter, the polarisation was changed and another loop was run.

Muon-spin relaxation

The μSR measurements were performed on the GPS spectrometer at the Paul Scherrer Institute in Switzerland. In these experiments spin-polarised positive muons are implanted in the sample. Each implanted muon decays (lifetime 2.2 μsec) emitting a positron preferentially in the direction of its spin polarisation at the time of decay. Using appropriately positioned detectors, one measures the asymmetry of positron emission as a function of time, $A(t)$, which is proportional to the time evolution of the muon spin polarisation. $A(t)$ depends on the distribution of internal magnetic fields and their temporal fluctuations. Further details on the μSR technique may be found in ref. 5.

Inelastic neutron scattering

Inelastic neutron scattering (INS) experiments were carried out using the direct-geometry time-of-flight neutron spectrometer IN5 located at the Institut Laue-Langevin, Grenoble, France. Approximately 1 g of crystalline material was loaded into a 10 mm-diameter double-wall, hollow aluminum cylinder. Spectra were acquired with incident neutron wavelengths of 3 Å, 4.8 Å and 6.5 Å at temperatures from 1.5 K to 15 K. The detector efficiency correction was performed using data collected from Vanadium and the background was subtracted. The data were processed and analysed using the LAMP program package.[6]

Density-functional theory calculations

Density-functional theory (DFT) calculations were performed on two levels of sophistication. To investigate the exchange coupling in complex **1** we considered the truncated model cluster [Dy(hfac)$_3$(NO$_3$)–CrF$_2$(py)$_4$]. Geometrical optimisation of this model cluster was performed using the VASP full-potential plane-wave code in scalar-relativistic approximation, in which pseudo-potentials together within the projector augmented wave method are used.[7] A kinetic energy cutoff of 400 eV was employed for the plane waves. For the DFT exchange-correlation functional the generalised gradient approximation (GGA) in the Perdew-Wang parameterisation[8] was used for the geometrical optimisation. A cubic simulation box of 30×30×30 Å^3 and the Γ point in reciprocal space were used. The magnetic properties of the optimised geometries as well as the experimental crystallographic structure were furthermore investigated using the atom-centered localized basis set approach as implemented in the NWChem package[9] in combination with hybrid functionals. In the latter calculations the segmented all-electron relativistic contracted basis sets for zeroth-order regular approximation (SARC-ZORA)[10] scalar-relativistic Hamiltonians were used for Dy and all-electron 6-31G* basis sets for all other atoms including Cr.

Isotropic magnetic exchange interactions were calculated within the localised basis set approach, using the hybrid meta-GGA M06-2X functional[11] in combination with applying the spin-polarized broken symmetry approach. The magnetic interaction of the model complex was expressed as $\hat{H} = -j\hat{\mathbf{S}}_{\mathrm{Dy}} \cdot \hat{\mathbf{S}}_{\mathrm{Cr}}$ where the exchange constant j can be extracted from the Noodleman-Ginsberg-Davidson expression[12] $j=2(E_{\mathrm{BS}}-E_{\mathrm{HS}})/S_{\mathrm{max}}^2$ (with E_{BS} the broken-symmetry energy and E_{HS} the high-symmetry energy). In the literature an alternative expression by Ruiz et al.[13] [$j=2(E_{\mathrm{BS}}-E_{\mathrm{HS}})/S_{\mathrm{max}}(S_{\mathrm{max}}+1)$] is popular and provides computationally better results in most cases. However no theoretical basis to prefer Ruiz et al.'s expression over the other one was established so far, therefore both expressions were explored here.

Spin-Hamiltonian simulations and fits

The spin-Hamiltonian simulations used to reproduce local and cluster magnetization curves, dc magnetic susceptibility and INS spectra are based on full diagonalization of the respective Hamiltonians. To take into account the powder nature of the sample, local and cluster magnetization curves were averaged over different directions of the magnetic field according to the equation

$$m_{i,\,\mathrm{powder}}(B) = \frac{1}{4\pi} \int_{\theta,\phi} \mathbf{m}_i(B,\theta,\phi) \cdot \mathbf{n}(\theta,\phi) \sin\theta \, d\theta \, d\phi \qquad \text{(S1)}$$

Here, $\mathbf{m}_i$ is the magnetic moment of element i, depending on the magnitude and orientation of the applied magnetic field which is expressed in spherical coordinates $\mathbf{B} = (B,\theta,\phi)$. Further, $\mathbf{n}$ is the unit

vector pointing along the *B*-field direction. This integral was realized numerically using a 16-point Lebedev-Laikov grid.[14] All fits shown in this work are least-squares fits which were obtained by minimizing the sum of squared deviations between the measured and calculated curves. The calculations were performed using home-written Matlab® and C codes.

Supplementary Information to the Results Section of the Main Article

Crystallography: Thermal ellipsoid plots of the crystal structures of 1 and 2

These plots indicate the thermal motion of the atoms in a molecule. Magnitude and anisotropy of the vibrations are coded as size and shape of the ellipsoids.

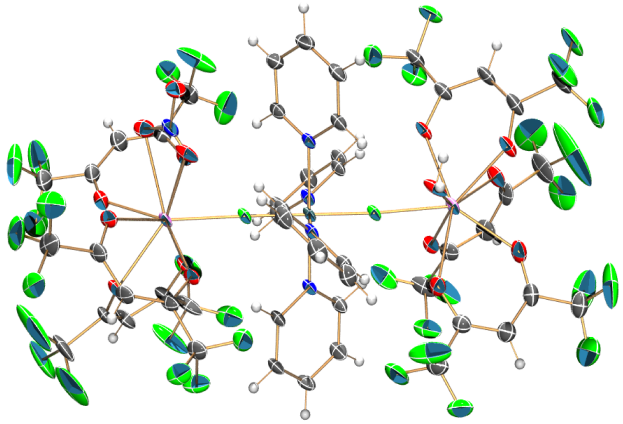

Fig. S1 Thermal ellipsoid plot (30% probability level) of **1**. Color code: pink: Dy, dark green: Cr, light green: F, red: O, blue: N, white: H.

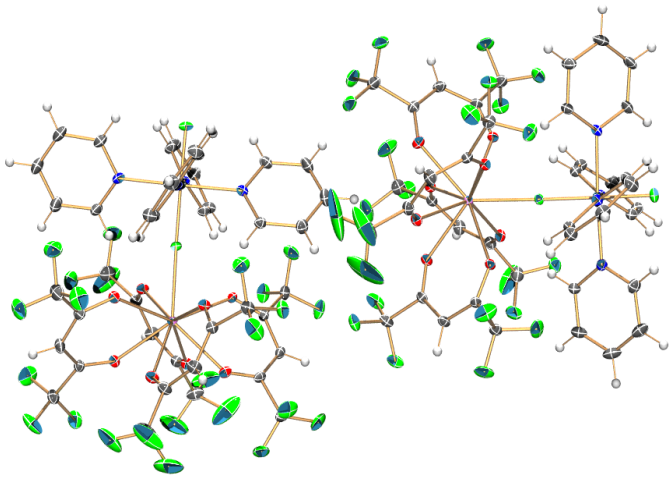

Fig. S2 Thermal ellipsoid plot (30% probability level) of **2**. Color code: pink: Dy, dark green: Cr, light green: F, red: O, blue: N, white: H.

X-ray absorption spectroscopy

XMCD is obtained following $I_{\mathrm{XMCD}}(E) = I_{+}(E) - I_{-}(E)$ where I_{+} and I_{-} refer to the X-ray absorption intensities for the two circular polarisations of the X-rays. The XMCD sum rules are given by[15]

$$\frac{\int_{\mathrm{M}_{4,5}} \mathrm{d}\omega(\mu^{+}-\mu^{-})}{\int_{\mathrm{M}_{4,5}} \mathrm{d}\omega(\mu^{+}+\mu^{-}+\mu^{0})} = \frac{1}{2}\frac{l(l+1)+2-c(c+1)}{l(l+1)(4l+2-n)}\langle L_z\rangle \qquad \text{(S2)}$$

$$\frac{\int_{\mathrm{M}_5} \mathrm{d}\omega(\mu^{+}-\mu^{-}) - \frac{c+1}{c}\int_{\mathrm{M}_4} \mathrm{d}\omega(\mu^{+}-\mu^{-})}{\int_{\mathrm{M}_{4,5}} \mathrm{d}\omega(\mu^{+}+\mu^{-}+\mu^{0})} = \frac{l(l+1)-2-c(c+1)}{3c(4l+2-n)}\langle S_z\rangle + \frac{l(l+1)[l(l+1)+2c(c+1)+4\,]-3(c-1)^2(c+2)^2}{6lc(l+1)(4l+2-n)}\langle T_z\rangle \qquad \text{(S3)}$$

Here, c, l and n denote the orbital quantum number of the core and the valence shell involved in the X-ray absorption process and the number of electrons in the valence shell, respectively. For the $M_{4,5}$ edges of the Dy^{III} ion, $c = 2$, $l = 3$ and $n = 9$. We replace $A = \int_{\mathrm{M}_{4,5}} \mathrm{d}\omega(\mu^{+}+\mu^{-}) = \frac{2}{3}\int_{\mathrm{M}_{4,5}} \mathrm{d}\omega(\mu^{+}+\mu^{-}+\mu^{0})$, $B = \int_{\mathrm{M}_5} \mathrm{d}\omega(\mu^{+}-\mu^{-})$, and $C = \int_{\mathrm{M}_4} \mathrm{d}\omega(\mu^{+}-\mu^{-})$ such that A is the integral over the XAS, and B and C are those over the XMCD across the Dy M_4 and M_5 edges as indicated for the integration range. The 2/3-factor in A takes into account the absorption of longitudinal polarization, which is not contained in our experimental XAS spectrum. However, because of the powder sample it can be set equal to the absorption of transverse polarization, justifying the simple calculation. $\langle T_z\rangle$ is the magnetic dipole operator. Since the 4f ions are very well described by L-S coupling and Hund's rules, and ligand fields have much weaker effects than in the 3d ions, $\langle T_z\rangle$ can be calculated analytically using eqs 8 and 9 in ref 15a, yielding a ratio of $\langle T_z\rangle / \langle S_z\rangle = -0.133$ for Dy^{III}.

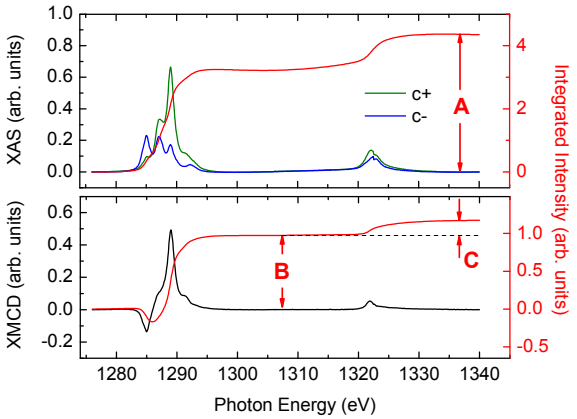

Fig. S3 (upper panel) X-ray absorption spectra on **1** at the Dy $M_{4,5}$ edges for the two indicated polarisations of the X-rays, recorded at 2 K and 6 T. The solid red line indicates the XAS integral. (lower panel) XMCD spectrum calculated from the data shown in the upper panel and XMCD integral.

To illustrate the sum-rules analysis, example X-ray absorption spectra on **1** along with the calculated XMCD spectrum are shown in Figure S3. The integral values *A*, *B* and *C* are indicated. The obtained spin and orbital as well as total magnetic moments for all measured spectra at different magnetic fields are summarized in Table S2. For high fields, "saturation" values between 5 and 6 μ_B are found for the total magnetic moment. In principle that would be in contradiction with the value of 10 μ_B expected from Hund's rules. However, the latter value would only be observed for an isotropic Dy^{III} ion in the absence of any ligand fields etc. The strong reduction compared to the free-ion value by a factor of ~2 originates from strong anisotropy. A calculation of the powder-averaged magnetic moment (using eqn S1) for a single Dy^{III} ion with only one Kramers doublet of $m_J = \pm 15/2$ yields a saturation magnetic moment of 5.0 μ_B. This is very close to the value observed by XMCD in our experiment.

Measurement	*B field* [T]	m_L [μ_B]	m_S [μ_B]	m_J [μ_B]
1	-1	-2.5(3)	-1.5(2)	-3.8(4)
2	+1	2.9(3)	1.6(2)	4.5(5)
3	-6	-3.5(4)	-2.1(2)	-5.6(6)
4	-6	-3.3(3)	-1.9(2)	-5.2(5)
5	+6	4.4(4)	1.6(2)	6.0(6)
6	+6	3.3(3)	1.9(2)	5.2(5)

Table S2. Values of the orbital and spin magnetic moments obtained for Dy using sum rules.

Ligand-field multiplet calculations

Multiplet calculations were carried out to simulate the X-ray absorption and X-ray magnetic circular dichroism for Dy^{III} and Cr^{III} using the TT-MULT program.[16] The results are shown in Figures 2b, 2d and 3b, 3d of the main text. For Dy the purely atomic calculation yields excellent agreement with the data. This is because the 4f levels are very localized, hence the X-ray absorption spectra at the $M_{4,5}$-edges of lanthanides are not very sensitive to ligand-field effects. Coulomb direct and exchange interaction are parameterised by Slater integrals, which were reduced to 60% of their atomic value for Dy^{III} and 80% for Cr^{III}. For Cr^{III} the calculation was done in D_{4h} symmetry with crystal field values of 10 Dq = 2.2 eV, Ds = –0.1 eV. Inclusion of ligand-to-metal charge transfer improves the agreement with the data. The charge transfer parameters used were $\Delta = 4$ eV, $T(A_1,B_1) = 2T(B_2,E)$ and $U_{dd} - U_{pd} = -1$ eV. Δ is defined as $E(d^{N+1}\underline{\mathbf{L}}) - E(d^N)$. In the final state of the X-ray

absorption process, the energy difference between the ionic and charge transfer configurations is given by $E(p^5d^{N+2}\underline{\mathbf{L}}) - E(p^5d^{N+1}) = \Delta + U_{dd} - U_{pd}$. T is the transfer integral between the metal d shell and the ligand p shell and is usually taken as being two times larger for the orbitals pointing along the bonding direction (A_1,B_1). At a field of –6 T, the expectation values $\langle S_z \rangle = -1.49$ and $\langle L_z \rangle = 0$ are found, in agreement with Cr^{III}. Simulations for both Cr^{III} and Dy^{III} were done considering a temperature of 2 K.

The above-mentioned parameters which were employed to simulate the Cr^{III} X-ray spectra can be compared to the values reported for $\{Cr^{III}F_2(py)_4\}^+$ in the literature.[17] From this, we obtain 10Dq = 2.3 eV, Ds = –0.125 eV and Dt = 0.0375 eV. These values are in excellent agreement with the parameters found from the multiplet calculations. Setting Dt = 0 in the calculations is justified because the observed X-ray absorption peaks are too broad (FWHM ~ 500 meV) to observe the associated energy splittings.

SQUID magnetometry

The temperature dependence of the in-phase component of the ac susceptibility of **1** is shown in Fig. S4 corroborating the SMM behaviour of **1**. Fig. S5 shows the magnetic-field dependence of the $\chi''(T)$ signal of **1** at a temperature of T = 1.8 K. At zero dc field the onset of a peak is visible but applying a small perturbing field further slows down magnetization relaxation.

The reduced magnetisation of **2** is shown in Fig. S6. The curves for different magnetic fields clearly do not superpose on each other, suggesting the presence of significant anisotropy and/or low-lying excited states. Fig. S7 shows the temperature dependence of χT of **2**. The room-temperature value of 15.5 cm^3 K mol^{-1} is consistent with the presence of a Dy^{III} ion with J = 15/2 (g_J = 4/3) and a Cr^{III} ion with S = 3/2 (g_S = 2) in the cluster, which would yield a theoretical value of 16.1 cm^3 K mol^{-1}. Between 300 K and 150 K the χT of **2** remains essentially constant, and below 50 K χT drops quickly. This may be due to the depopulation of ligand-field states of Dy^{III} and/or intracluster antiferromagnetic coupling. Ac magnetic measurements revealed no out-of-phase component ($\chi''(\nu_{ac})$ and $\chi''(T)$) above 1.8 K for **2** for all accessible static magnetic fields.

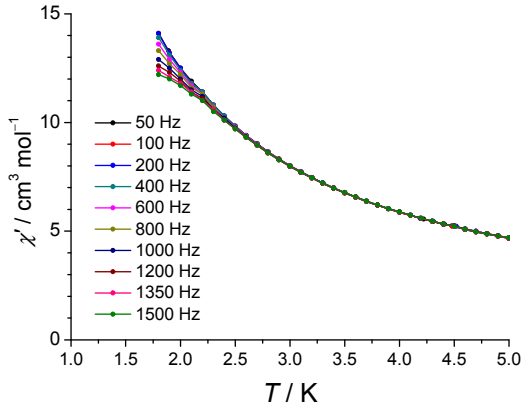

Fig. S4 In-phase component of the ac susceptibility of **1** as a function of temperature at selected frequencies of the oscillating magnetic field obtained with B_{dc} = 50 mT.

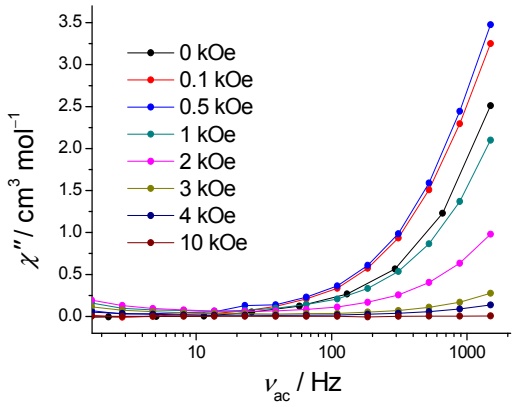

Fig. S5 Field dependence of the out-of-phase ac-susceptibility signal (χ'') for **1** measured at a temperature of 1.8 K.

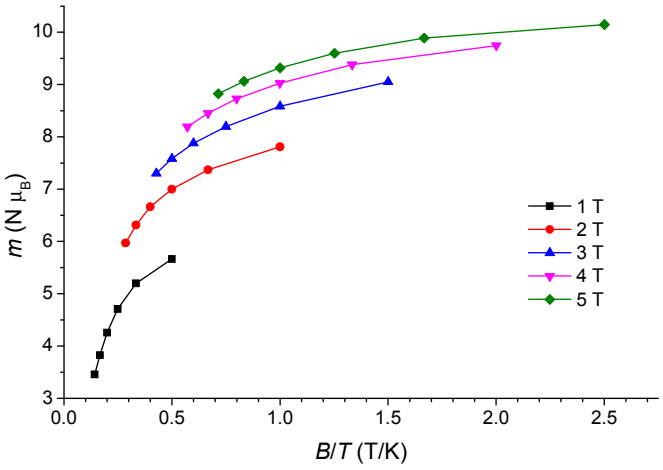

Fig. S6 Reduced magnetization of **2**. Solid lines are guides to the eye.

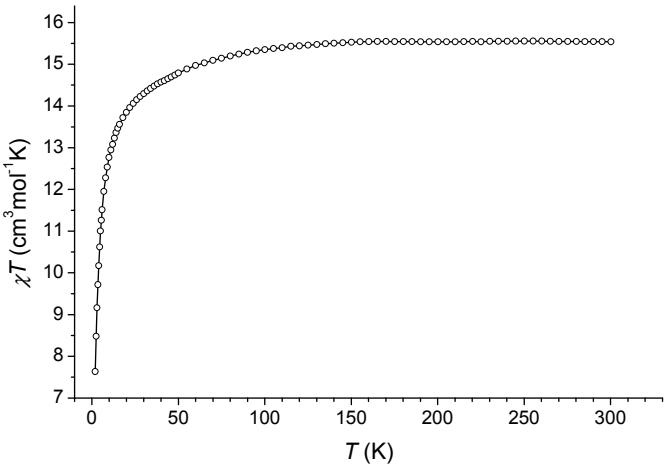

Fig. S7 Temperature dependence of the χT product of **2**. The solid line is a guide to the eye.

Inelastic neutron scattering

Information about the magnetic origin of INS features can be derived from their temperature and Q dependence. Upon increasing the temperature, magnetic excited energy levels become populated at the expense of ground-state-level population. This reduction of ground-state population leads to a decrease of INS transitions that correspond to excitation of the molecular magnet from the ground state to an excited state by a neutron, commonly referred to as "cold magnetic transition". In contrast, for harmonic vibrational modes the neutron energy loss response at a certain energy $E = \hbar\omega$ is proportional to the Bose factor[18] $1/[1 - \exp(-\frac{\hbar\omega}{k_B T})]$, which implies that the intensity can only stay constant or increase with increasing temperature. Furthermore, the Q-dependence contains relevant information, too. Here, Q is the absolute value of the momentum transfer, $Q = |\mathbf{Q}|$. At a constant energy E, for magnetic scattering the Q dependence is ruled by the magnetic form factors of the magnetic ions present in the cluster, and by their spatial coordinates.[19] Altogether, this leads to a decay of the scattering intensity with increasing Q. For incoherent scattering from vibrational modes the Q dependence is entirely different and the intensity is proportional to Q^2.[19]

In Figure 7a of the main text, features I and X were observed. Peak I appears at an energy of 3.4(2) cm^{-1} and possesses a full width at half maximum (FWHM) of 0.9 cm^{-1} which is close to that of the elastic peak of 0.8 cm^{-1}. The broad feature X is located at energy transfers from 9 to 16 cm^{-1}. Peak I shrinks with increasing temperature, while feature X is temperature independent. These features appear in the $S(Q,E)$ dependence shown in Figure S8, where they are indicated by black arrows. Whereas the scattering intensity $S(Q,E)$ at the energy of feature I decreases with Q, it exhibits opposite behaviour at the energy of the broad feature X. The latter is therefore proven to originate from a nonmagnetic excitation and can therefore be neglected in the further analysis of the magnetic properties of **1**. In contrast, feature I is inferred to be a cold magnetic transition.

The higher-resolution spectra shown in Fig. 7b of the main text reveal a three-fold splitting of feature I (energies 3.2(1), 3.7(1) and 4.3(1) cm^{-1}). The features Ia, Ib, Ic exhibit a linewidth of FWHM = 0.37 cm^{-1} which is equal to that of the elastic peak. The temperature dependence of features Ia-c suggests that they are all of magnetic origin. A closer look reveals that the temperature dependence of feature Ia is slightly weaker than that of Ib and Ic. Taking into account the small separation of 0.6 cm^{-1} between the peaks they can be attributed to transitions in the level scheme indicated in the inset of Fig. 7b. Further INS measurements at higher energy transfers do not reveal any other magnetic features up to an energy transfer of approximately 50 cm^{-1} as shown in Fig. S9.

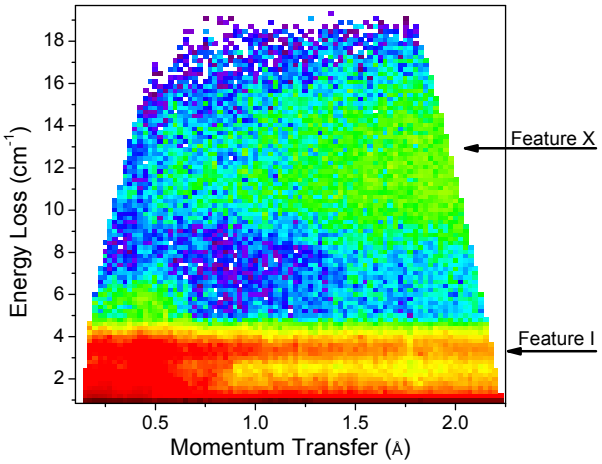

Fig. S8 Logarithmic plot of the $S(Q,E)$ dependence measured on **1** at a wavelength of λ = 4.8 Å and a temperature of 1.8 K. Red (violet) color represents strong (weak) intensity.

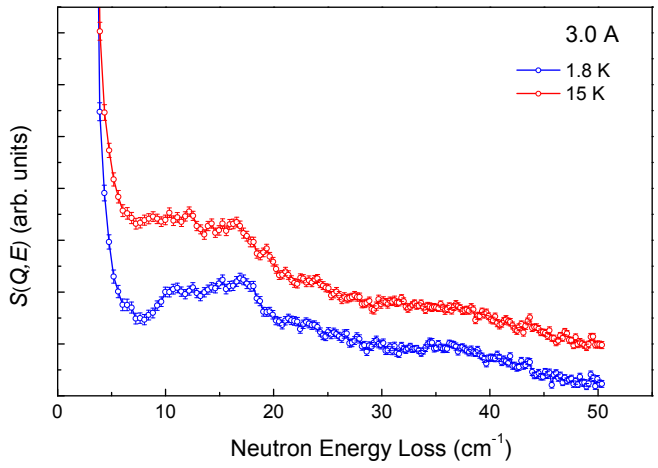

Fig. S9 INS spectra of **1** taken at a wavelength of λ=3 Å and temperatures as indicated in the plots. The intensity was summed for momentum transfers between 1.7 $Å^{-1}$ and 2.7 $Å^{-1}$. The curves were offset to improve visibility.

Muon-spin relaxation

The muon-spin relaxation data were analyzed using procedures similar as in ref. 20. Muon spin relaxation curves measured in zero magnetic field are presented in Figure S10. At low temperatures the asymmetry exhibits a dip within the first microsecond (inset of Figure S10), followed by a recovery and then relaxation at longer times. In contrast, at high temperature the asymmetry relaxes following an exponential curve. As discussed in ref. 20 the low-temperature relaxation curves are evidence that the internal magnetic field experienced by the implanted muons in **1** contains two contributions: a static component and a fluctuating component. Static (dynamic) fields are fields that fluctuate at a rate much slower (faster) than the muon lifetime of 2.2 μs. The static component is direct evidence of the slow relaxation of the magnetisation.

In the case of **1**, the asymmetry at all temperatures was found to fit best to a Lorentzian Kubo-Toyabe function multiplied by a square root exponential relaxation as represented by Equation 2 in ref. 20. The parameters λ and Δ extracted from the fits are shown in Figure S11. At high temperatures λ is small and $\Delta = 0$. Upon lowering the temperature λ increases strongly while Δ remains zero. At T^*~20 K, λ peaks and below this temperature Δ becomes non-zero. At lower temperatures λ further decreases and Δ saturates. The saturation values of 33 MHz correspond to a width in field of 40 mT. In analogy to ref. 20 the temperature-dependent relaxation time can be extracted as shown in Figure 6b in the main text. The relaxation time increases when the temperature is decreased but does not saturate down to 1.5 K, suggesting that the relaxation mechanism is thermally activated.

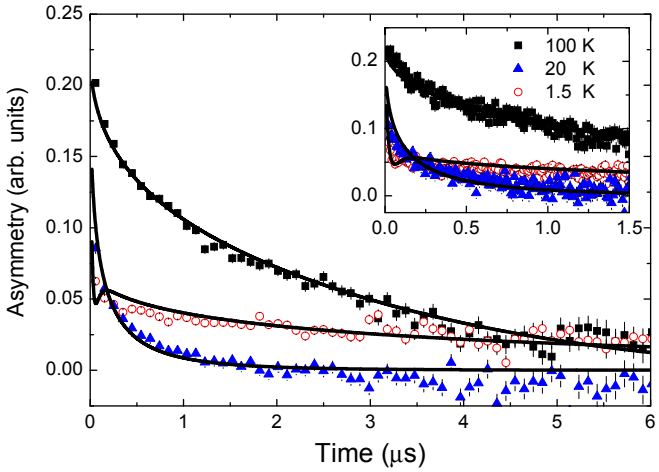

Fig. S10 Example muon-spin relaxation curves at three different temperatures. The inset shows a zoom into small timescales, where a clear dip in the relaxation can be seen at low temperatures, indicating the presence of static magnetic fields in the system.

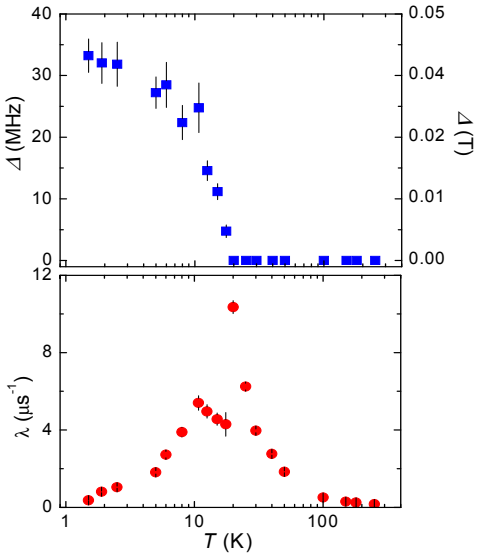

Fig. S11 λ (bottom) and Δ (top) obtained from fits to the relaxation curves as a function of temperature.

Spin-Hamiltonian models

A spin-Hamiltonian model is essential for extracting quantitive information from the data, such as the strength of the Dy-Cr exchange coupling. Our strategy was based on the following reasoning: On the one hand computationally efficient and simple models are needed. On the other hand it is desirable to reproduce a maximum of the experimental data. Furthermore, the number of free parameters typically decreases with decreasing complexity, mitigating problems of overparameterisation. Here we present the Hamiltonians following the order of decreasing complexity. The index i = 1,2,3 refers to the ion-site number within the trinuclear cluster, i.e. Dy(1)–Cr(2)–Dy(3). Details about the calculations are given on page 6 of the Experimental Section (ESI†). It is useful to start out with a spin Hamiltonian acting on the $J_1 = J_3 = 15/2$ ground multiplet of the Dy^{III} ions which we will refer to as *J-multiplet Hamiltonian*. The Cr spin takes the value $S_2 = 3/2$. The Hamiltonian is given by

$$\hat{H} = -j_{12}'\hat{\mathbf{J}}_1 \cdot \hat{\mathbf{S}}_2 - j_{23}'\hat{\mathbf{S}}_2 \cdot \hat{\mathbf{J}}_3 - j_{13}'\hat{\mathbf{J}}_1 \cdot \hat{\mathbf{J}}_3 + \sum_{i,k,q} B_{k,i}^q{}'\hat{O}_{k,i}^q \quad + \mu_B \sum_{i=1,3} g_i'\hat{\mathbf{J}}_i \cdot \mathbf{B} + \mu_B g_2'\hat{\mathbf{S}}_2 \cdot \mathbf{B} \qquad (S4)$$

The first two terms represent isotropic nearest-neighbour exchange couplings, and the third term is a much weaker coupling between the Dy^{III} ions. The fourth term describes the magnetic anisotropy induced by the ligand fields of the magnetic ions using Stevens operator notation. The last two terms represent the interaction with an applied magnetic field. Hamiltonian eqn S4 operates on the Hilbert space generated from the 16 states contained in each of the $J = 15/2$ multiplets of the Dy^{III} ions and another four states from the $S = 3/2$ multiplet of the Cr^{III} ion. Hence, the dimension of 1024 is fairly large. It is not only this dimension, which renders Hamiltonian eqn S4 rather impractical for

our simulations. More importantly, a vast number of magnetic anisotropy terms (for Dy: k = 2,4,6, q = –k, –k+1, ... +k) enter into the model because of the low symmetry of the two inequivalent Dy ligand fields. Hence, the very detailed model represented by Hamiltonian eqn S4 is strongly overparameterised, unless most of the free parameters would be determined by a dedicated series of additional measurements.

In order to significantly reduce the number of parameters we introduce a more practical Hamiltonian which operates in the restricted space of the ground state and the first-excited state Kramers doublets of each of the three ions. This *excited-state (encompassing) Hamiltonian* is given as eqn 1 of the main text. The terms are identical to those in the *J-multiplet* Hamiltonian but the number of anisotropy parameters is heavily reduced here. The maximally simplified Hamiltonian version is incorporated in the form of the spin-1/2 Hamiltonian given as eqn 2 of the main text.

We will now briefly discuss the interrelationship of the presented spin Hamiltonians eqns S4, 1 and 2. They describe the same magnetic system, which implies that there is a relation between spin-Hamiltonian parameters, e.g., j_{12}', j_{12} and $\mathbf{j}_{12,\mathrm{eff}}$. The same argument holds for anisotropy terms and **g**-matrices. Finding these relations is difficult in general, and in most cases the calculations can only be performed numerically. However, sometimes analytical relations can be derived with some approximations. Knowing such relations is useful. As an example, when the exchange coupling $\mathbf{j}_{12,\mathrm{eff}}$ in the spin-1/2 Hamiltonian has been determined which is rather simple because there are only a few free parameters, then j_{12} and j_{12}' can be readily calculated. This allows for consistent extensions of the basic spin-1/2 model to the more complex Hamiltonians.

Here, we focus on the relationship of g_i, $\mathbf{g}_{i,\mathrm{eff}}$, j_{ik}, and $\mathbf{j}_{ik,\mathrm{eff}}$ in eqs 1 and 2. A calculation using first-order quantum-mechanical perturbation theory treating the Zeeman term as the perturbation yields the following results, with $|m_{\mathrm{i,GS}}|$ the expectation value of the $\hat{J}_{i,z}$ operator for the ground state doublet of ion i = 1,3:

$$j_{12,\mathrm{eff},xy} = j_{12,\mathrm{eff},z} \cdot g_{1,\mathrm{eff},xy} / g_{1,\mathrm{eff},z} \qquad j_{23,\mathrm{eff},xy} = j_{23,\mathrm{eff},z} \cdot g_{3,\mathrm{eff},xy} / g_{3,\mathrm{eff},z}$$

$$j_{12,\mathrm{eff},z} = 2 j_{12} \, | m_{1,\mathrm{GS}} | \qquad j_{23,\mathrm{eff},z} = 2 j_{23} \, | m_{3,\mathrm{GS}} |$$

$$g_{1,\mathrm{eff},z} = 2 \, | m_{1,\mathrm{GS}} | \cdot g_J \qquad g_{3,\mathrm{eff},z} = 2 \, | m_{3,\mathrm{GS}} | \cdot g_J$$

(S5a-c)

If the ground-state Kramers doublets are eigenstates of the $\hat{J}_{i,z}$ operator (e.g. $m_{1,\mathrm{GS}} = \pm 15/2$), then the $j_{\mathrm{eff},xy}$ and $g_{\mathrm{eff},xy}$ terms will be zero. However, in non-uniaxial ligand fields the ground-state doublets can be admixtures (e.g. $|m_{1,GS}\rangle = \alpha|+15/2\rangle + \beta|-13/2\rangle$) and $j_{\mathrm{eff},xy}$ and $g_{\mathrm{eff},xy}$ can assume nonzero values.

Density-functional theory

Geometrical optimisation of the truncated model cluster as described on page 6 of the Experimental Section (ESI†) on the GGA level in scalar-relativistic approximation yields the Dy–F and F–Cr distances as 2.396 Å (exp. 2.321(2) Å) and 1.925 Å (exp. 1.903(2) Å). The non-bridging Cr–F distance is 1.862 Å (exp. in 2: 1.8440(15) Å and 1.8416(15) Å), the computed value is closer to that in the *trans*-$[CrF_2(py)_4]PF_6$ complex[21] (1.853(2) Å). The average Cr–N and Dy–O distances are 2.097 and 2.436 Å. The Cr–F–Dy bond-angle is 175.15° (exp. 176.49(13)°). Hence, the geometry is well reproduced.

References

[1] (a) J. Glerup, J. Josephsen, K. Michelsen, E. Pedersen and C. E. Schäffer, *Acta. Chem. Scand.*, 1970, **24**, 247, (b) M. F. Richardson, W. F. Wagner and D. E. J. Sands, *Inorg. Nucl. Chem.*, 1968, **30**, 1275.

[2] G. M. Sheldrick, *Acta Cryst.*, 2008, **A64**, 112.

[3] A. L. Spek, *PLATON, A Multipurpose Crystallographic Tool*, Utrecht University, Utrecht, The Netherlands, 2005.

[4] J. Krempasky, U. Flechsig, T. Korhonen, D. Zimoch, C. Quitmann and F. Nolting, *AIP Conf. Proc.*, 2010, **1234**, 705.

[5] S. L. Lee, S. H. Kilcoyne and R. Cywinski, *Muon Science;* SUSSP and Institute of Physics Publishing, 1998.

[6] (*a*) *LAMP, the Large Array Manipulation Program*. http://www.ill.fr/data_treat/lamp/lamp.html; (*b*) D. Richard, M. Ferrand and G. J. Kearley, *J. Neutron Research*, 1996, **4**, 33.

[7] (*a*) G. Kresse and J. Hafner, *Phys. Rev. B*, 1993, **47**, 558; (*b*) G. Kresse and J. Furthmüller, *Phys. Rev. B*, 1996, **54**, 11169; (*c*) P. E. Blöchl, *Phys. Rev. B*, 1994, **50**, 17953; (*d*) G. Kresse and J. Furthmüller, *Phys. Rev. B*, 1996, **54**, 11169.

[8] J. P. Perdew and J. Wang, *Phys. Rev. B*, 1992, **45**, 13244.

[9] M. Valiev, E. J. Bylaska, N. Govind, K. Kowalski, T. P. Straatsma, H. J. J. van Dam, D. Wang, J. Nieplocha, E. Apra, T. L. Windus and W. A. de Jong, *Comput. Phys. Commun.*, 2010, **181**, 1477.

[10] D. A. Pantazis, X.-Y. Chen, C. R. Landis and F. Neese, *J. Chem. Theory Comput.*, 2008, **4**, 908.

[11] Y. Zhao and D. Truhlar, *Theor. Chem. Acc.*, 2008, **120**, 215.

[12] (*a*) A. P. Ginsberg, *J. Am. Chem. Soc.*, 1980, **102**, 111; (*b*) L. Noodleman, *J. Chem. Phys.*, 1981, **74**, 5737; (*c*) L. Noodleman and E. R. Davidson, *Chem. Phys.*, 1986, **109**, 131.

[13] E. Ruiz, J. Cano, S. Alvarez and P. Alemany, *J. Comput. Chem*., 1999, **20**, 1391.

[14] V. I. Lebedev and D. N. Laikov, *Dokl. Math.*, 1999, **59**, 477.

[15] (a) P. Carra, B. T. Thole, M. Altarelli and X. Wang, *Phys. Rev. Lett.*, 1993, **70**, 694; (b) B. T. Thole, P. Carra, F. Sette and G. van der Laan, *Phys. Rev. Lett.*, 1992, **68**, 1943.

[16] (*a*) B. T. Thole, G. van der Laan, J. C. Fuggle, G. A. Sawatzky, R. C. Karnatak and J.-M. Esteva, *Phys. Rev. B*, 1985, **32**, 5107; (*b*) F. M. F. Groot, *Coord. Chem. Rev.*, 2005, **249**, 31.

[17] J. Glerup, O. Moensted and C. E. Schaeffer, *Inorg. Chem.*, 1976, **15**, 1399.

[18] G. Shirane, S. M. Shapiro and J. M. Tranquada, *Neutron Scattering with a Triple-Axis Spectrometer*, Cambridge University Press, Cambridge, England, 2002.

[19] (a) W. Marshall and S. W. Lovesey, *Theory of Thermal Neutron Scattering*, Oxford Clarendon Press, 1971; (b) Furrer, A., Güdel, H. U. *Phys. Rev. Lett.* **1977**, *39*, 657; (c) Waldmann, O. *Phys. Rev. B* **2003**, *68*, 174406.

[20] Z. Salman, S. R. Giblin, Y. Lan, A. K. Powell, R. Scheuermann, R. Tingle, and R. Sessoli, *Phys. Rev. B*, 2010, **82**, 174427.

[21] G. Fochi, J. Strähle and F. Gingl., *Inorg. Chem.*, 1991, **30**, 4669.